Enhanced densification and conductivity of LAMGPB glass-ceramic electrolyte through ultra-fast high-temperature sintering

Journal of Power Sources 640 (2025) 236768

Contents lists available at ScienceDirect

Journal of Power Sources

journal homepage: www.elsevier.com/locate/jpowsour

Enhanced densification and conductivity of LAMGPB glass-ceramic electrolyte through ultra-fast high-temperature sintering

Sofia Saffirio [a], Antonio Gianfranco Sabato [b], Daiana Marcia Ferreira [b], Albert Tarancón [b,c], Claudio Gerbaldi [a,*], Federico Smeacetto [a,**]

[a] Department of Applied Science and Technology, Politecnico di Torino, C.so Duca Degli Abruzzi 24, 10129 Torino, Italy
[b] IREC- Institut de Recerca en Energia de Catalunya, Jardins de Les Dones de Negre, 1, 2[a] Pl., Barcelona, 8010, Spain
[c] ICREA, Passeig Lluís Companys 23, Barcelona, 8010, Spain

HIGHLIGHTS

- NASICON-type systems can be pressure-less sintered in 3 min by UHS.
- Density values achieved by UHS are comparable to conventional sintering.
- UHS preserves lithium and prevents the formation of secondary phases.
- The ionic conductivity of LAMGPB is doubled compared to commercial LAGP.
- B_2O_3 addition enhances grain boundary conductivity, particularly under UHS treatment.

GRAPHICAL ABSTRACT

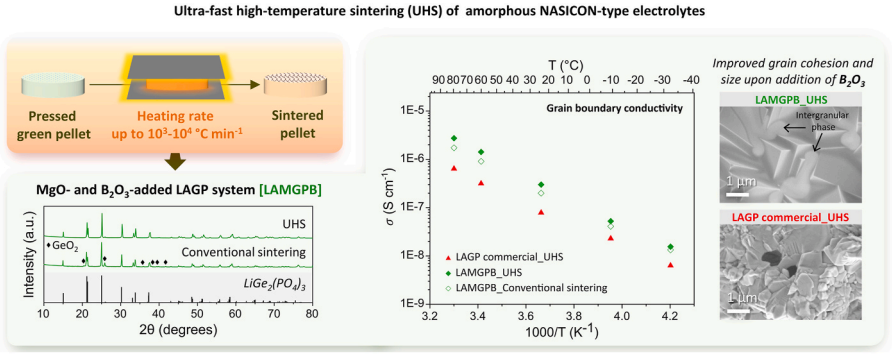

ARTICLE INFO

Keywords:
NASICON-Type electrolyte
Glass-ceramic
Ultrafast high temperature sintering
UHS
Grain boundary conductivity
Lithium battery

ABSTRACT

The promising use of NASICON-type ceramics electrolytes highlights the need for rapid, energy-efficient and scalable ceramic processing. Ultra-fast high-temperature sintering (UHS) overcomes the limitations of conventional sintering including prolonged times, high energy demand and lithium volatilization, which can adversely affect ionic conductivity and structural stability. Here, UHS is investigated for the sintering of a modified $Li_{1.5}Al_{0.3}Mg_{0.1}Ge_{1.6}(PO_4)_3$ + 0.5 wt% B_2O_3 composition (namely, LAMGPB) obtained through melt-casting, in comparison with a commercial LAGP counterpart. The densification, crystallization behavior and microstructural evolution of the two amorphous systems are investigated across increasing currents. Results demonstrate that the high heating rates achieved through UHS promote rapid densification and enable the formation of a fully crystalline and pure LAGP ion-conducting phase in both systems. Electrochemical impedance spectroscopy reveals an enhanced total ionic conductivity for LAMGPB compared to commercial LAGP. A reduced grain boundary resistance is indeed observed for this system, attributed to the improved grain size and cohesion induced by the segregation of amorphous B_2O_3 at the grain boundary. Overall, this study sheds light on the

* Corresponding author. author.
** Corresponding author.
E-mail address: sofia.saffirio@polito.it (S. Saffirio).

https://doi.org/10.1016/j.jpowsour.2025.236768
Received 7 January 2025; Received in revised form 24 February 2025; Accepted 9 March 2025
Available online 13 March 2025

correlations between the crystal phase evolutions, microstructural features and electrochemical performances of NASICON-type systems, unravelling the effect of UHS sintering and oxide doping on these aspects.

1. Introduction

The growing demand for high-performance energy storage solutions has spurred significant interest in the development of solid-state batteries (SSBs). On paper, SSBs offer higher energy density compared to conventional liquid electrolyte-based batteries [1]. Moreover, SSBs are intrinsically safer and more sustainable, as they utilize solid electrolytes that are non-volatile [2], non-flammable [3] and less hazardous, thus mitigating risks associated with the use of liquid electrolytes, such as leakage, flammability, and instability under high temperatures as well as use of toxic solvents/components.

Among the various solid electrolyte materials, NASICON-type glass-ceramics are receiving increasingly high attention by the academic/industrial research community in the field due to their promising features, particularly $Li_{1.5}Al_{0.5}Ge_{1.5}P_3O_{12}$ (LAGP) has [4,5]. However, the traditional sintering processes used to densify LAGP, and ceramic materials in general, require long thermal treatments (dwelling time 10–12 h) at high temperatures (700–900 °C) to achieve high densification [6,7]. This, in addition to relatively slow heating/cooling rates typically allowed by conventional furnaces (1–20 °C min^{-1}), leads to total thermal cycles that can last for days. Indeed, traditional sintering is a high energy-demanding process, which concurrently leads to undesirable lithium volatilization due to the prolonged exposure of materials to high temperatures. As a result, their stoichiometry is altered, leading to the formation of insulating secondary phases that impact on the ionic conductivity of the resulting materials [8].

To address these challenges, various alternative sintering techniques have been explored, such as cold sintering, microwave-assisted sintering and spark plasma sintering (SPS). These methods offer potential solutions by reducing sintering times and high-temperature exposure, thereby mitigating lithium volatilization and enhancing ionic conductivity [9–11]. Nevertheless, they retain a material-specific applicability, enable limited geometries and require complex equipment, which can restrict their broader adoption. Microwave-assisted sintering of ceramics for example often depends on the microwave absorption properties of the materials [12,13], and the SPS technique requires the use of dies to compress the ceramic while sintering [14], which makes it more difficult to sinter specimens with complex three-dimensional (3D) structures [15].

In this context, ultrafast high-temperature sintering (UHS) has gained attention as a revolutionary technique capable of overcoming the drawbacks of both conventional and existing rapid sintering methods. Introduced by Wang et al., in 2020, it represents a significant advancement in the field of ceramic processing, particularly for the sintering of superionic conducting solid electrolytes like LAGP [15]. This technique stands out for its ability to achieve rapid densification of ceramics within seconds to minutes, as opposed to hours required by traditional methods [16–26]. The fundamental principle of UHS involves sandwiching the green ceramic body between two carbon felts, which are then crossed by high electrical currents, thus enabling rapid heating through the Joule effect. Through this approach, ultrafast sintering with heating rates up to 10^5 °C min^{-1} can be achieved, minimizing the risk of volatilization of relevant atoms, e.g. lithium, and thereby preserving the desired material composition and properties. Moreover, UHS is versatile in terms of atmospheric conditions, as it can be adapted to operate in various atmospheres (e.g., inert, reducing), thus further broadening its applicability [27,28]. In comparison to other rapid sintering techniques, heating rates are controllable and faster reaching up to ~10^3–10^4 °C min^{-1} and maximum temperatures as high as 3000 °C are easily achieved. In addition, faster sintering times (1–10 s) are enough to achieve densification, and requirements on the samples are minimal, making it a general sintering method. Indeed, the UHS technique enables the sintering of complex ceramic structures and the co-sintering of multilayered structures. Importantly, UHS provides heat to the samples in a very localized way, without the need to inefficiently heat voluminous furnaces. This, in addition to the minimal times required per process, drastically reduces the energy consumption compared to conventional thermal treatments, accounting for a strong reduction of the carbon-footprint associated with conventional ceramic production.

Different studies have been reported on the sintering of NASICON-type electrolytes through UHS [29–32], which demonstrate good densification and reduced lithium loss, resulting in absence of secondary insulating phases and ionic conductivities in line with the relevant works reported in the literature for the same materials sintered in conventional furnaces.

The overall ionic conductivity of ceramic electrolytes is strongly influenced by the ionic transport processes occurring at the grain/grain interface. In the literature, the effect of adding sintering aids to LAGP to improve its grain cohesion has been already widely investigated by the scientific community, proving significant enhancements on systems obtained through conventional thermal treatments [2,33–38].

Within this context, understanding the influence of sintering aids on LAGP systems processed via UHS is of significant interest to advance the knowledge of the scientific community on this emerging technique. In this regard, Curcio et al. [30] explored the UHS sintering of commercial LAGP amorphous powders mixed with 1 wt% B_2O_3 from two different precursors (B_2O_3 and Li_3BO_3). Differently, the present work investigates the UHS sintering of an in-house made LAGP-based glassy system (namely LAMGPB) where B_2O_3 is directly incorporated into the glass matrix. This is achieved by stoichiometrically mixing H_3BO_3 with the other precursors for melt-casting. The LAMGPB system has been previously studied by the authors in its bulk form and upon conventional thermal treatment, demonstrating improved grain cohesion and ionic conductivity through the addition of B_2O_3 with respect to other sintering aids, including Y_2O_3 and SiO_2, on an Mg-added LAGP composition [39]. Here, the effect of UHS sintering on the crystal phase, microstructural and ion conduction features of LAMGPB is investigated to unravel its potential in comparison with commercial LAGP.

2. Experimental

2.1. Materials and methods

The designed composition $Li_{1.5}Al_{0.3}Mg_{0.1}Ge_{1.6}(PO_4)_3$ + 0.5 wt% B_2O_3 (namely LAMGPB), consisting in 18.3Li_2O-3.7Al_2O_3-2.4MgO-39GeO_2-36.6P_2O_5 + 0.7B_2O_3 (mol%), was produced through melt-casting, specifically by melting the precursors at 1350 °C for 1 h and casting the produced glass on a brass plate. An extensive description of the precursors and the conditions used for the melt-casting is provided in our previous work [39], where the effect of different oxide doping was investigated on the LAMGPB system in its bulk form. To sinter this system through UHS, in the present study the cast bulk glass was milled for 2 h and then sieved below 25 μm using an automatic sieve (Endecotts, Octagon 200 Sieve Shaker). The particle size distribution of the produced powders (d50 = 9.3 μm, d90 = 33.9 μm) is shown in Fig. S1, *Supplementary Information* section. As a benchmark, a comparison with commercial LAGP was carried out. Specifically, commercial LAGP amorphous powders, namely LAGP-comm, (d50 = 5.5 μm, d90 = 11.9 μm) were provided by Toshima Manufacturing Co., Japan.

For the sintering through UHS, both types of amorphous powders were die-pressed for 2 min at a pressure of 6 MPa to produce pellets with

13 mm diameter. UHS was carried out inside a glove-box under a controlled nitrogen atmosphere. Two graphite felt strips (10.5 mm in length, 20 mm in width and 5 mm in thickness, provided by AvCarb®, USA) were placed and tightened between two copper electrodes, in their turn connected to a DC power supply (EA-PSI 9080-60 T, Elektro-Automatik, Germany). Increasing currents of 19, 20, 21, 22 and 23 A were applied for 180 s to evaluate their effect on the properties of the LAGP-comm and LAMGPB systems, which include crystallization, microstructure and ionic conductivity. A thermocouple was placed at the center of the carbon strips to record the temperature throughout the treatments and to determine the maximum temperature reached for each sample. No controlled cooling ramp was applied and this step was carried out naturally for all the samples, without compromising their structural integrity. For direct comparison, the same amorphous powders were die-pressed under the same conditions provided above and then subjected to conventional sintering at 700 °C for 12 h.

2.2. Characterization

Laser light scattering was performed on the LAMGPB and LAGP amorphous powders after milling and sieving to determine their particle size distribution.

The shrinkage and thermal behavior of both LAGP-comm and LAMGPB upon heating were investigated through Hot Stage Microscopy (HSM, Hesse Instruments, Heating microscope EM301) and Differential Scanning Calorimetry (DSC, 404 F^3 Pegasus®, Netzsch, Germany), respectively. HSM was carried out at a heating rate of 5 °C min^{-1}, while DSC was carried out at increasing heating rates, specifically at 5/10/20/40/50 °C min^{-1}. The maximum heating rate investigated through DSC was set as a safety limit for the instrument.

The crystalline structure of the sintered materials was assessed by X-ray diffraction (XRD, Bruker D8 ADVANCE, Germany) with Cu Kα radiation (λ = 1.5406 Å) analysis using Cu Kα radiation at a voltage of 40 kV and a current of 40 mA. The diffractograms were collected in the 2θ range of 10–80°.

The relative density *d* of the sintered samples was calculated as the ratio of their absolute density value, determined through the Archimedes method, to the reference theoretical density value of LAGP, i.e. 3.42 g cm^{-3}.

Cross-sections of the pellets were analyzed through Field-Emission Scanning Electron Microscopy (FESEM) using a ZEISS Auriga system (equipped with a 30 kV Gemini FESEM column, Germany) in high vacuum at a voltage of 5 KV. Thin lamellas of sintered LAGP-comm and LAMGP were extracted from the corresponding pellets by means of dual beam system given by a scanning electron microscope (SEM) coupled with a Xe + ion plasma-FIB (Solaris X from Tescan). The lamellas were thereafter analyzed through transmission electron microscopy (TEM) and energy-dispersive X-ray spectroscopy (EDX) employing a Talos F200X G2 (Thermo Scientific) system.

Electrochemical impedance spectroscopy (EIS) was performed using gold as blocking electrodes to assess the ionic conductivity of the electrolytes at different temperatures. The sintered pellets were polished and sputtered with Au on both sides, and then mounted on a Linkam stage (Linkam Scientific Instruments, UK) equipped with an LNP95 (Linkam Scientific Instruments, UK) liquid nitrogen pump. EIS was carried out at increasing temperatures, from −35 to 80 °C. The registered spectra were fitted using the RelaxIs software (rhd instruments GmbH & Co.). To this purpose, two resistance (R) and constant-phase element (CPE) blocks in series were employed to distinguish the bulk (R_b, CPE_b) and grain boundary (R_{gb}, CPE_{gb}) contributions at high and low frequency, respectively. The total resistance was determined as $R_{tot} = R_b + R_{gb}$, and the total ionic conductivity, σ_{tot}, was calculated as:

$$\sigma_{tot} = \left(\frac{t}{AR_{tot}}\right) \quad \text{eq. 1}$$

where *t* denotes the thickness and *A* the surface area of the samples. The activation energy (E_a) for Li^+-ion conduction was calculated as the slope of the Arrhenius plot $\ln(\sigma_{tot})$ *vs* $1000/T$ as follows:

$$\ln\sigma\left(\sigma_{tot}T\right) = \ln a - \left(\frac{E_a}{RT}\right) \quad \text{eq. 2}$$

Here, *a* is a pre-exponential factor and R is the universal gas constant.

The conductivity of the bulk σ_b was calculated according to equation (2) by substituting R_{tot} with R_b.

For the grain boundary conductivity instead, the brick-layer model (BLM) was applied:

$$\sigma_{gb} = \left(\frac{1}{R_{gb}}\right)x\left(\frac{t}{A}\right)x\left(\frac{\delta}{D}\right) \quad \text{eq. 3}$$

where D is the size of grains and δ their grain boundary thickness, assuming the electrolyte as an assembly of bricks.

As the dielectric constant for the bulk and grain boundary is generally assumed as equal for LAGP, the following relationship holds:

$$\left(\frac{\delta}{D}\right) = \left(\frac{C_b}{C_{gb}}\right) \quad \text{eq. 4}$$

where C_b and C_{gb} are the bulk and grain boundary capacitances, calculated as $C = Q^{1/n} \times R^{(1/n)-1}$ (Q and n are parameters of the CPE obtained from fitting). Based on this relationship, the conductivity of the grain boundary was calculated as follows:

$$\sigma_{gb} = \left(\frac{1}{R_{gb}}\right)x\left(\frac{t}{A}\right)x\left(\frac{C_b}{C_{gb}}\right) \quad \text{eq. 5}$$

As the discrimination between the bulk and grain boundary contribution became less accurate at increasing temperatures due to the curve shift towards high frequencies, σ_{gb} was calculated and plotted up to 30 °C.

3. Results and discussion

3.1. Thermal characterization

Thermal characterization was conducted to investigate the thermal behavior of LAGP-comm and LAMGPB amorphous powders. In particular, hot-stage microscopy (HSM) was employed to investigate their shrinkage behavior upon heating, while differential scanning calorimetry (DSC) was utilized to determine their characteristic temperatures, including glass transition (T_g), crystallization onset (T_x) and crystallization peak (T_p) temperatures.

These investigations are crucial for gaining insights on the densification and crystallization mechanisms of a given amorphous system [40,41]. At temperatures above the glass transition temperature (T_g), the activation of viscous flow in the glassy particles facilitates densification. As the temperature continues to rise, crystallization initiates at the onset temperature (T_x), reaching its maximum crystallization rate at the peak temperature (T_p). To achieve an effective sintering, these two processes must be decoupled, meaning that the system should possess a good glass-stability (i.e. $\Delta T = T_x - T_g$) [42]. The greater ΔT, the more stable the glass, meaning that the viscous flow of particles is not hindered by crystallization.As LAGP NASICON-type systems are of interest in this work, it is noteworthy to underline that their glass stability is low (about 80–90 °C) compared to other glass-ceramic systems [43].

DSC curves at a heating rate of 5 °C min^{-1} and the corresponding characteristic temperatures are shown in Fig. 1 and Table 1, respectively. According to the results, the characteristic temperatures of LAMGPB (Fig. 1b) are shifted towards lower values compared to commercial LAGP-comm (Fig. 1a), presumably as a result of the addition of MgO and B_2O_3 within the glass composition [44,45]. In particular, T_g, T_x and T_p values of 482, 572 and 591 °C, respectively, are registered for

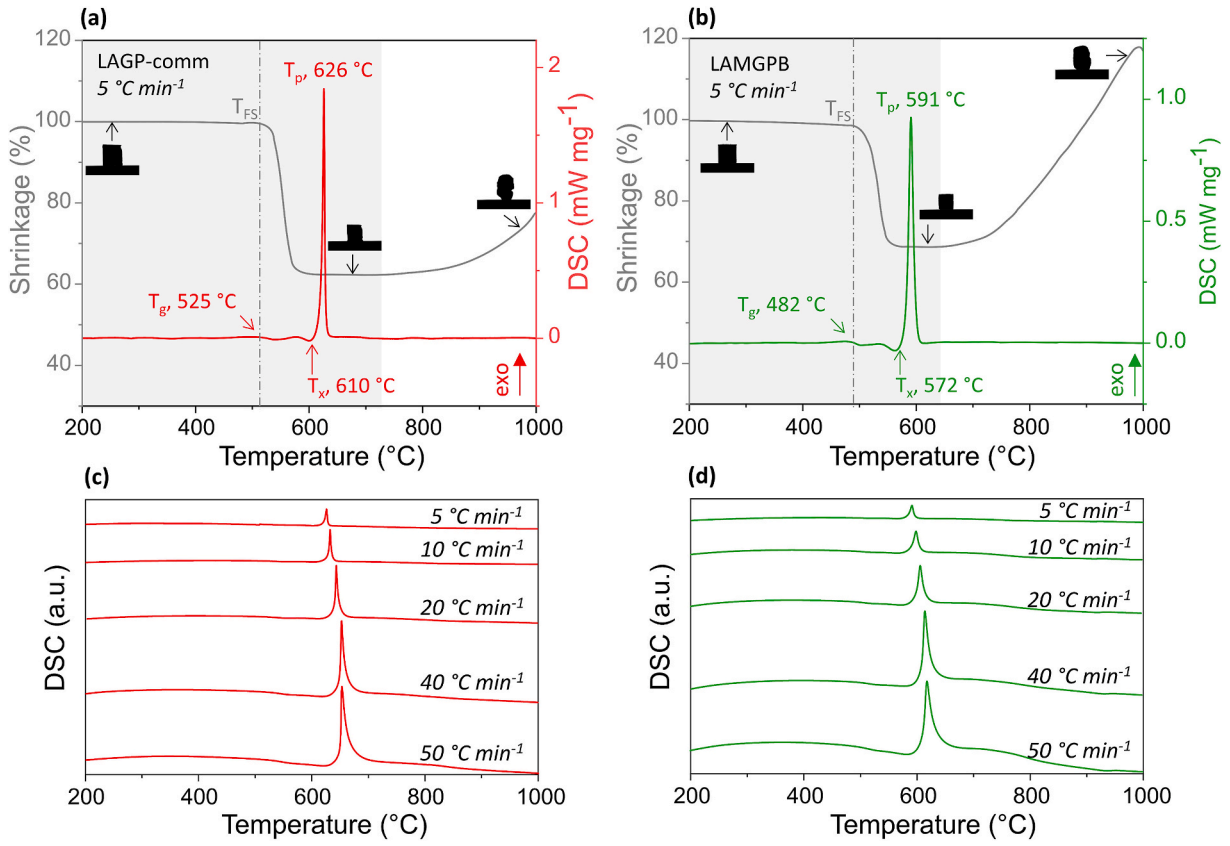

Fig. 1. DSC curves and HSM shrinkage behavior of LAGP-comm **(a)** and LAMGPB **(b)** amorphous powders at a scanning rate of 5 °C min^{-1}. The powders were pressed into small pellets for HSM analysis. DSC was also carried out at 5/10/20/40/50 °C min^{-1} to evaluate the effect of increasing heating rates on the thermal stability (T_x-T_g) of LAGP-comm **(c)** and LAMGPB **(d)** amorphous powders in view of their sintering through UHS.

Table 1
Characteristic temperatures (°C) extrapolated from the DSC curves of amorphous LAGP-comm and LAMGPB powders at increasing heating rates (from 5 to 50 °C min^{-1}). The glass-stability T_x-$T_{g,on}$ is also calculated.

Scan rate (°C min^{-1})	LAGP-comm				LAMGPB			
	$T_{g,on}$ (°C)	T_x (°C)	T_p (°C)	T_x-$T_{g,on}$ (°C)	$T_{g,on}$ (°C)	T_x (°C)	T_p (°C)	T_x-$T_{g,on}$ (°C)
5	525	610	626	85	482	572	591	90
10	525	615	632	90	485	578	600	93
20	525	624	642	99	485	584	607	99
40	526	630	650	104	487	593	612	106
50	529	637	653	108	490	602	616	112

LAMGPB compared to 525, 610 and 626 °C for LAGP-comm. The value of T_p for LAMGPB is lower also compared to the value (641 °C) recorded in our previous study for the same system, under the same heating rate, but in a bulk rather than powder form [39]. This suggests that the LAMGPB system undergoes surface-driven crystallization, in agreement with the findings reported by Pershina et al. [45] for B_2O_3-doped LAGP compared to undoped LAGP.

However, despite the downward shift of the characteristic temperatures upon addition of B_2O_3, ΔT results in Table 1 indicate a higher glass stability for this system compared to LAGP-comm, with a T_x - T_g value of 90 *vs.* 85 °C, respectively. Despite the presence of MgO (a glass modifier) in the glass structure, the enhanced stability of LAMGPB can be attributed to the incorporation of B_2O_3 into the glass network as a glass former [40], resulting in a more tightly packed structure with superior thermal stability [46].

As fast heating influences glass-ceramic materials by shifting their characteristic temperatures towards higher values [47], densification and crystallization are expected to be decoupled when the materials are exposed to ultra-fast heating during UHS. For this reason, DSC measurements at increasing heating rates (from 5 to 50 °C min^{-1}, as allowed by our DSC equipment) have been carried out for both commercial LAGP-comm and amorphous LAMGPB powders (Fig. 1c and d), to investigate the evolution of their glass stability and discuss the expected sinter-crystallization behavior when treated through UHS. The characteristic temperatures and glass stability at all heating rates are also reported in Table 1 for both systems. According to the data, T_g is not significantly affected by the increasing heating rate, in agreement with previous studies reported in the literature [48]. Indeed, an increase of only 4 °C (from 525 to 529 °C) is observed for LAGP-comm, while an 8 °C-shift from 482 to 490 °C is registered for LAMGPB, when passing from 5 to 50 °C min^{-1}. The starting temperature for densification and nucleation is therefore not significantly affected by the heating rate to which the material is subjected. On the contrary, T_x and T_p values related to crystallization are strongly influenced by the heating rate: a shift of T_x from 610 to 637 °C, and from 572 to 602 °C is observed for LAGP-comm and LAMGPB, respectively, from 5 to 50 °C min^{-1}. Therefore, as expected, the glass stability T_x-T_g of both systems is increased with the increasing heating rate, reaching 108 and 112 °C, respectively, at 50 °C min^{-1}. Notably, LAMGPB retains an enhanced glass stability compared to LAGP-comm across the range of investigation. The stability of both systems is expected to further increase if we consider the heating rate reached through UHS. During our synthesis, in fact, 500 °C were approximately reached after around 50 s of treatment, corresponding to a heating rate of about 10 °C s^{-1}, *i.e.* 600 °C min^{-1}. At this heating rate, the glass stability of both systems is projected to further increase, shifting T_x values towards significantly higher temperatures. Noteworthy, results for LAGP-comm are well aligned with the

values previously reported by Curcio et al. [30] at 5, 10 and 50 °C min^{-1} for a batch of the same material provided by Toshima, indicating a good reproducibility among different studies. Small differences of approximately 2–3 °C are in fact observed in the T_g, T_x and T_p values for a given heating rate compared to our findings.

As a combination of thermal analysis and microscopy, HSM enables to visualize the shrinkage behavior of a system upon heating. By combining this information with the thermal response previously detected through DSC, it is therefore possible to visualize the coupling or decoupling of the densification and crystallization processes for a given glass-ceramic system. Shrinkage profiles at 5 °C min^{-1} are shown in Fig. 1 and characteristic figures of the pellets are provided within the plots at the shrinkage stages of interest (initial state, sintering plateau, final state). According to the profile of LAGP-comm (Fig. 1a), shrinkage starts at 525 °C. This temperature also corresponds to the value of T_g previously detected through DSC (Table 1) and associated to the activation of the viscous flow for densification. For the same system, a maximum shrinkage of 38 % is reached at 610 °C. As crystallization initiates at this exact temperature according to DSC, densification and crystallization for LAGP-comm are not properly decoupled, as also indicated by the low glass stability reported at 5 °C min^{-1} for this system. Most likely, densification ends at 610 °C due to the starting of crystallization that inhibits the viscous flow required for further sintering. Indeed, the viscosity of a crystallized glass is significantly higher than the parent glass, thus limiting the viscous flow [49]. When considering LAMGPB (Fig. 1b), shrinkage starts at 485 °C (T_g is equal to 482 °C) and reaches its maximum at 565 °C. As crystallization starts at 572 °C according to DSC, LAMGPB shows a slightly improved glass stability at 5 °C min^{-1} compared to LAGP-comm, in accordance with the previous results. However, due to its larger average particle size (Fig. S1), LAMGPB shows a lower shrinkage extent compared to LAGP-comm (38 %), reaching a maximum shrinkage of 31 % (Table 2). These results suggest that the sinter-crystallization behavior of an amorphous system can be exhaustively elucidated through DSC only when it possesses a low glass stability. When the glass stability is high, HSM is instead fundamental to identify the temperature of maximum shrinkage and its decoupling from T_x.

The shrinkage behaviors evaluated at 5 °C min^{-1} and plotted in Fig. 1 are not representative for the two systems when subjected to fast heating through UHS. At the estimated heating rate of 600 °C min^{-1}, T_{FS} is expected to remain almost unchanged compared to 5 °C min^{-1}, given the little shift registered for T_g at increasing heating rates. Contrarily, as the onset of crystal growth T_x is markedly shifted towards higher temperatures, LAGP and LAMGPB powders are projected to densify up to those temperatures, accordingly. However, this would not necessarily result in an increased shrinkage extent: a high heating rate would lead to a shift of T_x that might enable to reach the maximum possible densification before crystallization; however, the same heating rate might also not provide enough time to achieve that densification before reaching T_x. As densification involves the coalescence of particles, kinetics plays a pivotal role on its achievement [50]. For this reason, it would be of significant interest to evaluate how increasing heating rates influence the extent of shrinkage in NASICON-type systems.

Despite the shrinkage values reached at the plateaus, both systems exhibit a post-plateau swelling resulting in volume increase and, therefore, density reduction. This swelling behavior is not unusual in glassy systems and is likely due to the trapping of gasses occurring during their melt-casting [51].

Table 2
Maximum shrinkage (%) extrapolated from the HSM curves of amorphous LAGP-comm and LAMGPB powders pressed into small pellets and analyzed at 5 °C min^{-1}.

	LAGP-comm	LAMGPB
Max. Shrinkage (%) at 5 °C min^{-1}	38	31

For LAMGPB, swelling initiates at approximately 630 °C (40 °C above the crystallization peak T_p) and the sample exceeds its initial area at around 850 °C. At 1000 °C, a 50 % swelling with respect to the plateau (and 20 % with respect to the initial state) is reached. In contrast, LAGP-comm remains stable up to 730 °C (103 °C above T_p), reaching a 15 % swelling at 1000 °C with respect to the plateau. The significant difference in swelling onset temperatures and swelling extent between LAGP-comm and LAMGPB can be ascribed to differences in their production processes: industrial *vs.* laboratory scale, respectively. Along with the extent of gas trapping within the glass structure, the production process of a glass determines also its characteristic temperatures [52], as well as the particle size distribution of the resulting amorphous powders.

Overall, as the glass stability of NASICON-type systems increases with the increasing heating rate, fast treatments such as UHS enable not only to reduce energy consumptions but also to decouple the densification and crystallization processes, therefore enabling improved sintering efficacy of these systems with respect to conventional sintering at low heating rates. Regardless of the sintering technique, attention should be paid to the swelling behavior of amorphous NASICON-type glassy systems upon heating.

3.2. Crystal phase and microstructural characterization

After gaining insights into the sinter-crystallization mechanism of the starting amorphous powders through thermal analyses, the densification and crystallization of LAGP and LAMGPB were studied from a physical, microstructural and morphological point of view after UHS treatments. In particular, the result of applying different currents during UHS was investigated, from 19 to 23 A, to reach increasing maximum temperatures up to nearly 700 °C, as estimated by the use of a thermocouple placed between the felts. Unfortunately, a precise evaluation of the temperature reached by the samples cannot be provided due to the intrinsic limitations of the UHS setup. The precise measurement of temperature represents indeed a significant challenge in the context of non-conventional sintering techniques, such as UHS [53]. This challenge regards both the experimental setup and the approaches used for temperature evaluation. As pellets are positioned between two carbon felts and Joule heating is produced when electric current flows, the bending of the felts at the edges can impact their effective power dissipation in the first place. Furthermore, they tend to lose contact with the sample during sintering, leading to uneven temperature distribution, especially in thicker samples [54]. In addition to this, the thickness of the sample significantly affects the temperature gradient across its cross-section, and the shrinkage that occurs during sintering introduces further uncertainties on its temperature evaluation [54]. The thermal capacity and emissivity of the sample and its contact conditions with the felts also influence its overall thermal evolution [21]. Thermocouples used for temperature detection should be shielded to prevent effects related to the applied current field, as they are usually inserted between the felts and positioned in close proximity to the sample, as in the current study. However, due to the high thermal conductivity (orders of magnitude higher) of the metal tip compared to the carbon felts, the use of thermocouples can significantly underestimate the sample temperature – even in the steady state of UHS – as a result of heat dispersion, and the uncertainty of the temperature estimation remains quite wide [53]. Temperature values are anyway fundamental to describe a sintering process. Indeed, as the current is highly dependent on the specific UHS experimental setup, it does not adequately represent the treatment undergone by a pellet. For this reason, in the figures and discussion of the present work, approximate temperature values recorded by the thermocouple are reported alongside the amperages. For a more comprehensive perspective, the temperature profiles recorded over time for both systems and at increasing currents are available in the supplementary information section (Fig. S2).

In this manuscript, results are mainly shown for the samples treated at 20 and 22 A, as relevant representatives of the structural and

microstructural evolutions occurring at increasing temperatures for both LAGP-comm and LAMGPB. The progressive densification and crystal phase formation can be observed from the X-ray diffractograms and the FESEM micrographs shown in Figs. 2 and 3, respectively. For a comprehensive overview of the results collected in the full 19–23 A range, the reader is instead referred to Figs. S3 and S5 and to Tables S2 and S3, in the *Supplementary Information Section,* also including an evaluation of the crystallized volume fraction (α) and crystallite sizes (D) via Rietveld method (Fig. S4 and Table S1). A comparison with the effects of conventional sintering is also carried out and discussed for both systems.

Fig. 2 shows a comparison among LAGP-comm and LAMGPB before UHS treatment (*i.e.* as-received and as-cast, respectively) and after UHS treatment (at 20 A and 22 A, corresponding to approximately 595 °C and 670 °C for LAGP-comm, respectively, and to 565 °C and 595 °C for LAMGPB, respectively). At the given currents, the different temperature values recorded for LAGP-comm and LAMGPB can be ascribed to the low temperature control resulting from the criticalities mentioned above. Digital photographs of UHS-treated pellets are also provided in the insets of Fig. 2. Both starting materials possess a fully amorphous structure, LAGP as-received by Toshima and LAMGPB as-cast in our laboratory, indicating a successful glass-casting process for the latter. When pressed into pellets and subjected to UHS treatment at 19 A for 180 s, both systems begin to densify while still retaining a fully amorphous structure (Figs. S3 and S5). This indicates that a temperature T above T_g – which allows viscous flow for sintering – and below the onset of crystallization T_x has been reached, *viz.* $T_g < T < T_x$. A relative density of 82 and 89 % is measured for LAGP-comm and LAMGPB, respectively

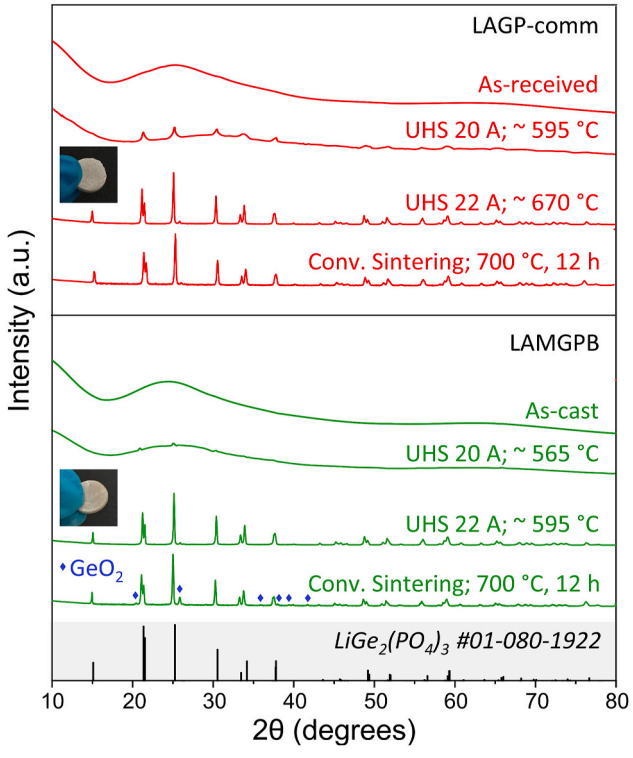

Fig. 2. Comparison on the X-ray diffractograms of LAGP-comm and LAMGPB amorphous powders before and after UHS treatment, showing the progressive crystallization of the powders at increasing applied currents. The temperature values reached at the end of the UHS treatments and measured through a thermocouple are reported alongside the corresponding applied currents. Digital pictures of the pellets treated through UHS at 22 A for 180 s are shown in the insets. A comparison with the X-ray diffractograms resulting from conventional sintering (700 °C, 12 h) is also provided for both systems. The reference pattern of the main $LiGe_2(PO_4)_3$ crystalline phase is reported underneath.

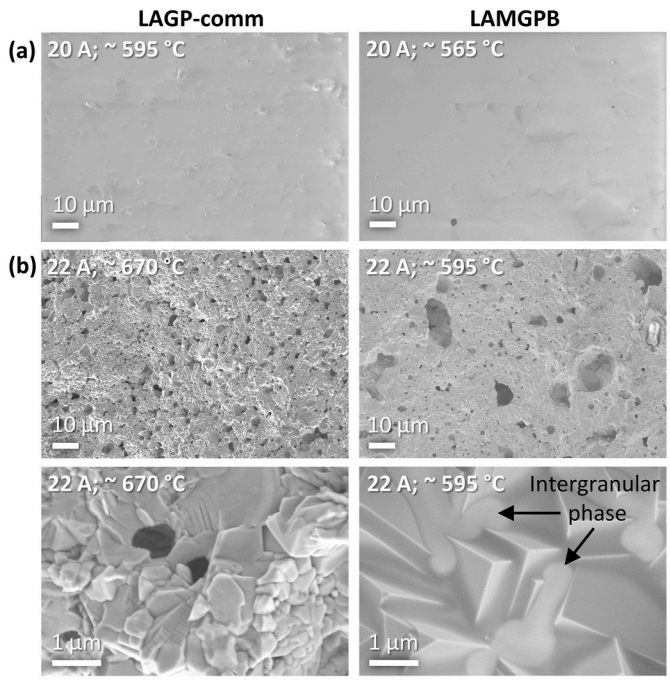

Fig. 3. FESEM micrographs of LAGP-comm and LAMGPB amorphous powders sintered through UHS at 20 A (~565 °C and ~595 °C, respectively) **(a)** and at 22 A (~595 °C and ~670 °C, respectively) at two different magnifications **(b)**.

(Tables S2 and S3).

By increasing the current to 20 A, close-to-full densification of the two systems is achieved, reaching relative density values of 87 and 91 %, respectively; the structures are still predominantly amorphous (Fig. 3a) and the $LiGe_2(PO_4)_3$ (LGP) crystalline phase begins to crystallize in both systems, as evidenced by the low-intensity main peaks of LGP starting to appear on the amorphous halo of the corresponding XRD diffractograms. In particular, the starting crystallization is more pronounced in LAGP-comm. This might be easily attributed to the different temperatures values reached by the two systems according to the detecting thermocouple. However, given the wide uncertainty on the evaluation of UHS temperature, also the smaller particle size (and consequently the enhanced specific surface area and reactivity) of LAGP-comm in comparison to LAMGPB powders (see Fig. S1 on PSD) has to be considered, along with the difference in their T_g and T_x as a result of adding B_2O_3 glass former. Overall, it can be posited that a temperature approaching T_x is reached at 20 A. A comparison on the different crystal phase evolution of LAGP and LAGP + B_2O_3 treated through UHS cannot be carried out between our study and the one by Curcio et al. [30], as X-ray diffractograms at increasing currents were not reported in their work. At 21 A, the X-ray diffraction patterns of LAGP-comm and LAMGPB exhibit narrow high-intensity peaks; their relative height is consistent with the reference pattern of LGP (JCPDS: 01-080-1924; major reflections at 25.159°, 21.307° and 21.477°), indicating the complete crystallization of the two systems into the Li-ion conducting phase, at a temperature above T_x. Based on the UHS temperature evaluations, neither system is expected to be crystalline under the applied current: at 21 A, the thermocouple recorded maximum temperatures of ~615 °C for LAGP-comm and of ~585 °C for LAMGPB. However, DSC measurements indicated that the crystallization temperatures T_x for these materials were already equal to 637 °C and 602 °C, respectively, at a heating rate of 50 °C min^{-1}. Under UHS treatment these T_x values are expected to shift to higher temperatures, as heating occurs at 600 °C min^{-1}. Eventually, these findings suggest that the reported temperature values should be interpreted as indicative. The formation of a crystalline microstructure at 21 A is also supported by FESEM analysis (Fig. S5), concurrently evidencing the appearance of pores compared to the well-densified

glassy pellets treated at 20 A. Crystallization implies the rearrangement of atoms from a disordered to an ordered and well-packed structure [55]. Curcio et al. [28] attributed the formation of pores exclusively to this density change. In the present study, however, the formation of pores aligns closely also with the swelling behavior observed through HSM analysis *(Paragraph 3.1)*, which is likely the primary factor responsible for the extensive pore formation observed. A decreased relative density value of 81 and 87 % was measured for LAGP-comm and LAMGPB, respectively, compared to 20 A. No secondary phases are detected in both systems when crystallized through UHS at 21 A, in contrast to conventional sintering, where GeO_2 is formed as an insulating secondary phase in LAMGPB (Fig. 2). In the diffractograms, an overall shift (0.042° for LAGP-comm and 0.052° for LAMGPB) of the diffraction peak positions towards lower angles is observed with respect to the pattern of LGP, as a result of the partial substitution of Ge^{4+} with Al^{3+} (and also with Mg^{2+} for LAMGPB) in the LGP crystal lattice. Indeed, Rietveld refinement carried out on LAMGPB in our previous study [39] revealed an enlargement of the *a* and *c* cell parameters upon addition of MgO with respect to standard data of LAGP, suggesting the effective substitution of Ge^{4+} with Mg^{2+}, which also results in a doubled number of free lithium ions for conduction compared to Al^{3+}. On the other hand, B_2O_3 was not expected to enter the crystal lattice but rather to segregate at the grain boundary in the form of amorphous oxide, and this was confirmed by the negligible lattice distortion observed. These results can be found in Tables 2 and in the Supplementary Information of the cited study.

Notably, the absence of secondary phases is also confirmed upon the UHS treatment of LAGP-comm and LAMGPB at 22 A, reasonably thanks to the rapid treatment that enables to limit lithium loss, preventing the formation of the related secondary phases such as GeO_2 and $AlPO_4$. This result significantly highlights the positive contribution of using UHS. At 22 A, the relative density value of LAGP-comm decreases to 77 %, while that of LAMGPB reaches a value of 84 %. At 23 A, a further decrease to 72 and 80 % is observed, respectively. At this current, LAGP-comm still retains a pure LGP crystalline phase while $Li_6Ge_2O_7$ (JCPDS: 01-075-1524; major reflections at 20.886°, 21.259° and 25.944°) is formed in LAMGPB. To our knowledge, this phase was not previously observed in LGP systems. The structure and transport properties of $Li_6Ge_2O_7$ as a Li-ion conducting electrolyte were reviewed by Burmakin et al., in 1991 [56] and a conductivity of 8.0×10^{-7} S cm^{-1} at RT was expected for this phase by Laskowski et al., in 2023 [57]. As the main reflections of $Li_6Ge_2O_7$ appear as a shift of the main reflections of LGP, we suppose that it might have segregated as a non-equilibrium phase inside LAMGPB treated at 23 A due to the ultra-fast heating and cooling reached during UHS. The presence of Li in its composition confirms that the $Li_6Ge_2O_7$ crystalline phase does not result from lithium volatilization, as it typically occurs upon prolonged treatment times during conventional sintering. This is further confirmed by the absence of GeO_2 and $AlPO_4$.

It is noteworthy to highlight that the XRD diffraction pattern of the LAMGPB sample treated at 23 An also evidences the appearance of a halo, indicating the formation of an amorphous phase (Fig. S3). This phase is not observed in samples treated at lower currents, suggesting that its formation is attributable to the elevated temperature achieved during the treatment, coupled with the rapid cooling rates, which effectively freeze the generated amorphous structure. It is not clear to the authors whether the appearance of the $Li_6Ge_2O_7$ secondary phase and of the amorphous phase are related. However, a glassy surface aspect can be observed through visual inspection of all the LAGP and LAMGPB samples treated at 21 A and above (Fig. S6a). FESEM investigations indeed reveal a transition from a dense surface layer to a porous bulk in all the crystalline samples (Fig. S6b). This inhomogeneity is likely a consequence of the temperature gradient to which pellets are subjected across their thickness during UHS treatment [54]. Notably, although the high cooling rates reached during cooling (about 400 °C min^{-1}) are uncommon in ceramics and could have potentially induced cracks due to thermal shock, the samples analyzed in this study remained intact, as evidenced by Fig. 2, also in agreement with other observations reported in the literature [58–60].

Further insights into on the X-ray diffractograms discussed above are provided by Rietveld method (Fig. S4 and Table S1). For the LAGP-comm samples, the evolution of crystallized volume fraction (α) indeed reveals a clear trend of increasing crystallinity (94, 98, 100 %) with the applied current (21, 22, 23 A, respectively), culminating in complete crystallization. Importantly, no residual glassy phase is detected in the LAGP-comm sample treated at 23 A. The crystallite sizes, ranging between 200 and 300 nm, align well with the FESEM images. In the case of the LAMGPB samples, a fully crystallized state is instead achieved when the current increases from 21 A (α = 91 %) to 22 A (α = 100 %). However, a further increase to 23 A leads to the formation of an additional phase and reduces the degree of crystallization (down to 80 %), as discussed above. Additionally, in LAMGPB samples, the crystallite size increases with the applied current – from 200 nm at 21 A to 600 nm and 700 nm for the 22 A and 23 A samples, respectively. This confirms an increase in the average grain size compared to LAGP-comm, in agreement with FESEM observations.

From a wider perspective, currents above 21 A lead to a progressive decrease in the relative density values of both LAGP-comm and LAMGPB samples. In particular, LAMGPB shows higher densities compared to LAGP-comm at all currents (Tables S2 and S3). FESEM micrographs of the two systems upon crystallization (Fig. 3b) evidence the formation of small and abundant widespread voids in LAGP-comm *vs.* large and localized voids in LAMGPB, at all currents (Fig. S5). According to the density values discussed above and reported in Tables S2 and S3, widespread voids appear more detrimental for densification compared to localized voids, despite being smaller in size. At higher magnifications (Fig. 3b), FESEM micrographs show the presence of an intergranular phase with an amorphous aspect that enhances grain cohesion compared to LAGP-comm and induces the formation of large (1–2 μm) squared-like grains in the LAMGPB samples. A further investigation through TEM and EDX analysis of LAMGPB sintered via UHS (Fig. 4a) confirms the presence of this intergranular phase (area 2, dashed lines), well penetrated among the crystalline grains. Its corresponding elemental composition (plotted into a stacked histogram) shows an increased concentration of Mg and a decreased Ge and Al content, compared to the surrounding crystalline grains (area 1, dashed lines). Unfortunately, due to their low atomic numbers, Li and B could not be effectively detected through EDX. However, the analysis allows to exclude the segregation of $AlPO_4$ and GeO_2, in agreement with the previous XRD analysis, as well of $Li_6Ge_2O_7$. The excess Mg detected in the intergranular phase therefore segregates at the grain boundaries and does not lead to the formation of Mg-containing crystalline secondary phases (in agreement with XRD), most likely thanks to the presence of amorphous B_2O_3. Indeed, B_2O_3 is an amorphous oxide that does not enter the crystal lattice of LGP and melts at about 450 °C, accounting for enhanced grain cohesion and promoting grain growth. The amorphous phase and the improved microstructure previously observed through FESEM can therefore be attributed to the to the addition of B_2O_3 and MgO. Further TEM analysis (Fig. 4b) supports the amorphous nature of this phase, evidencing the sharp interfaces and reduced cohesion typically observed at the interface with a crystalline secondary phase, such as GeO_2. Notably, this insulating phase appears exclusively in the microstructure of LAMGPB processed via conventional sintering, in line with the XRD results shown in Fig. 2. Eventually, a comparative analysis of the two sintering routes (top-left micrographs of Fig. 4a and b) demonstrates that the microstructure achieved through UHS sintering of LAMGPB in 180 s is comparable to that obtained via conventional sintering of the same material a 700 °C for 12 h. This confirms that ultra-fast heating effectively facilitates densification and crystal growth within a significantly reduced processing time.

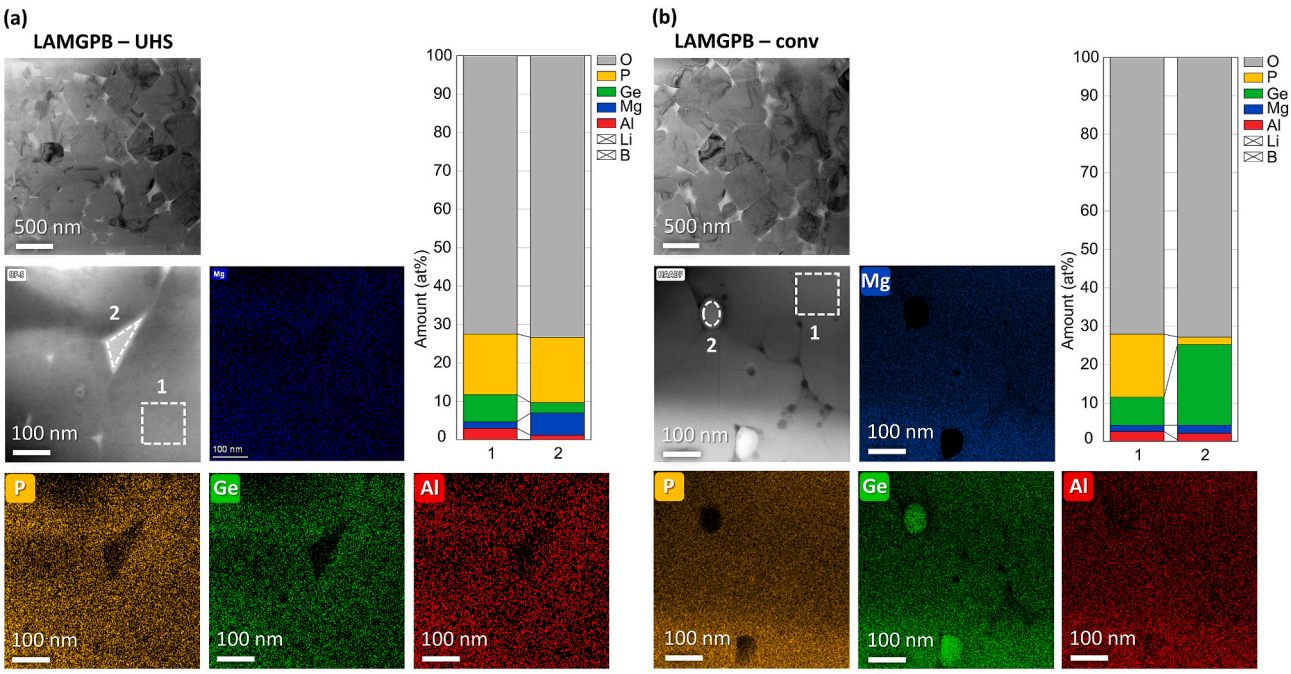

Fig. 4. TEM micrographs of LAMGPB treated via UHS **(a)** and via conventional sintering **(b)** evidencing a comparable morphology between the two samples (top-left in both figures). Corresponding TEM-EDX micrographs (below) show the elemental mapping and composition: of the secondary phase with an amorphous aspect observed through FESEM analysis (Fig. 3), which segregated at the grain boundaries in LAMGPB as a result of compositional modifications compared to LAGP-comm; of GeO_2 crystalline secondary phase, which formed exclusively in LAMGPB upon conventional sintering, in agreement with previous XRD results (Fig. 2).

3.3. *Electrochemical Impedance Spectroscopy analysis*

Electrochemical Impedance Spectroscopy (EIS) was carried out between −35 and 80 °C to evaluate the effect of UHS on the Li^+-ion conduction of LAGP-comm and LAMGPB upon sintering through UHS. Based on the crystalline and morphological characterization discussed above, only the samples that crystallized at 21, 22 and 23 A were electrochemically characterized, as the transport of lithium ions is hindered in amorphous NASICON-type structures [61]. The Nyquist and Arrhenius plots are fully discussed below for the samples treated at 22 A, which showed the most promising results, while a comparison in terms of ionic conductivity values among all the crystalline samples is provided in Tables S2 and S3 and discussed at the end of this paragraph.

Nyquist plots and corresponding fitting curves of representative EIS at increasing temperatures are shown in Fig. 5. Plots at low temperatures (−35, −20, 0 °C) are shown separately from plots at higher temperatures (from 20 to 80 °C). Specifically, results are reported in Fig. 5a and c for LAGP-comm, and in Fig. 5b and d for LAMGPB, both treated at 22 A.

The spectra at low temperatures are constituted by two depressed arcs, corresponding to two different transport phenomena: one at high frequencies related to bulk transport, and one at low frequencies related to grain boundary transport. The inclined straight line at low frequencies is instead related to electrode polarization, *i.e.* to the blocking and accumulation of ions occurring at the interface between the electrolyte and the metal blocking electrodes. For comparison, the plots were normalized to the geometrical factor t/A of the samples, where t and A are thickness and area of the sample, respectively. As a result, resistance values are reported as kΩ*cm. In the plots, each depressed arc is fit by the parallel combination of a resistance R (indicating the resistance to Li^+ ion transport) with a constant phase element CPE (representing the capacitance generated by dipole and double-layer formation at the bulk and grain boundary, respectively [62]). A single constant phase element CPE is instead used to fit the inclined straight line at low frequencies. The circuit used to fit the spectra at low temperatures is therefore constituted by a series combination of three blocks, as illustrated in Fig. S7a. Through the fitting, the bulk and grain boundary resistances (R_b and R_{gb}) of a given sample can be evaluated by determining the intercept of the high-frequency and low-frequency arcs with the real impedance axis. The total resistance R_{tot} is calculated as the sum of R_b and R_{gb}, that also corresponds to the intercept of the inclined straight line with the real axis. In the case of a symmetric configuration with blocking electrodes, in fact, the intercept of the bulk arc approaches the origin of the axis (0,0), as no further transport phenomena occur at high frequencies. Since resistance decreases and transport phenomena fasten with the increasingtemperature, at 20 °C arcs are significantly shifted towards lower values on the real axis (*i.e.* lower resistances and higher frequencies), no longer enabling to detect the bulk arc as being outside of the frequency range allowed by the measuring equipment. For this reason, the spectra at 20 °C and above are constituted by an inclined straight line and a single depressed arc, modelled using a two-block circuit (Fig. S7b) to determine R_b and R_{gb}.

As evidenced by the amplitude of the arcs in the normalized plots, LAMGPB possesses a markedly decreased grain boundary resistance and an increased bulk resistance compared to LAGP-comm at all temperatures. At −20 °C for example, values of R_{gb} of about 180 and 500 kΩ cm and of R_b equal to 80 and 60 kΩ cm were obtained for LAMGPB and LAGP-comm, respectively, from fitting. The lower grain boundary resistance of LAMGPB is attributed to the improved grain cohesion resulting from the presence of B_2O_3 in the glass-composition, as previously evidenced in Fig. 3 and discussed in *Paragraph 3.3*. The increased bulk resistance is instead likely due to lithium loss during the glass-casting process, even though an excess amount of lithium precursor was added to compensate for the expected loss. Despite the higher bulk resistance, however, the decreased R_{gb} value of LAMGPB enables to achieve a lower R_{tot} compared to LAGP-comm at all temperatures, in agreement with the intercepts of the inclined straight lines. This results in a higher ionic conductivity of LAMGPB, as shown by the Arrhenius plots of the total conductivities *vs.* 1000/T in Fig. 5e. Specifically, LAMGPB shows values that are doubled compared to LAGP-comm, *viz.* 5.3×10^{-6} and 6.6×10^{-5} S cm^{-1} at −20 and 20 °C, respectively, compared to 2.1×10^{-6} and 3.4×10^{-5} S cm^{-1} for LAGP-comm at the same temperatures (Table 3). The separate contribution of bulk and

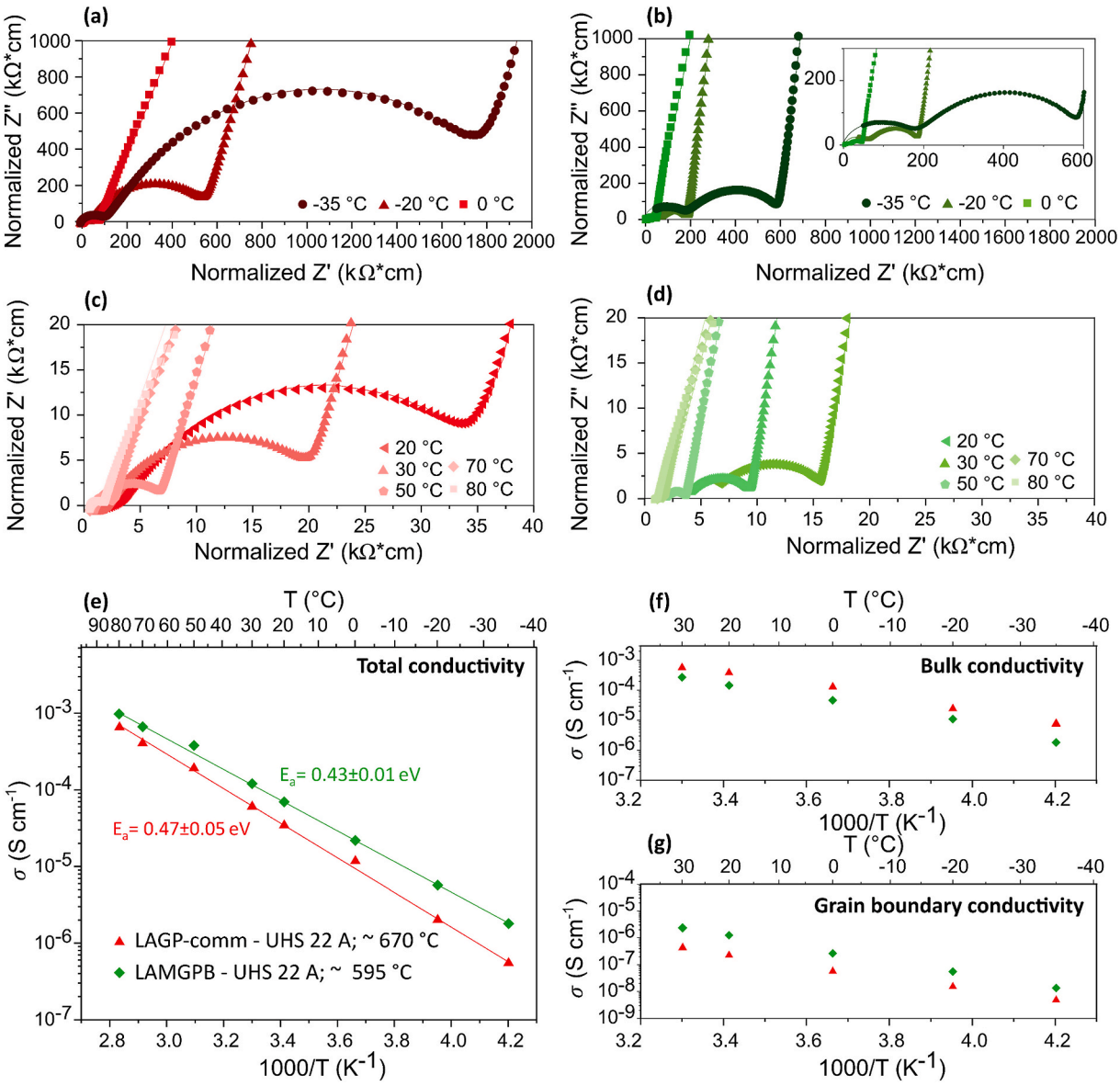

Fig. 5. Nyquist plots between −35 and 0 °C of LAGP-comm **(a)** and LAMGPB **(b)**; Nyquist plots at temperatures between 20 and 80 °C of LAGP-comm **(c)** and LAMGPB **(d)**. LAGP-comm is represented in shades of red, LAMGPB in shades of green. Both samples were sintered through UHS at 22 A for 180 s. Corresponding Arrhenius plots of the ionic conductivity data *vs* 1000/T are compared for the two systems, specifically the total **(e)** bulk **(f)** and grain boundary **(g)** ionic conductivity. (For interpretation of the references to colour in this figure legend, the reader is referred to the Web version of this article.)

Table 3
Total, bulk and grain boundary conductivity values (S cm^{-1}) measured at −20 and 20 °C for LAGP-comm and LAMGPB amorphous powders sintered through UHS at 22 A. The activation energy for the two systems is also reported.

Sample	Ionic conductivity @ −20 °C (S cm^{-1})			Ionic conductivity @ 20 °C (S cm^{-1})			E_a (eV)
	σ_{tot}	σ_{bulk}	σ_{gb}	σ_{tot}	σ_{bulk}	σ_{gb}	
LAGP-comm 22 A	2.1 × 10^{-6}	2.2 × 10^{-5}	2.0 × 10^{-8}	3.4 × 10^{-5}	3.5 × 10^{-4}	3.2 × 10^{-7}	0.47 ± 0.05
LAMGPB 22 A	5.3 × 10^{-6}	1.5 × 10^{-5}	5.2 × 10^{-8}	6.6 × 10^{-5}	1.7 × 10^{-4}	1.4 × 10^{-6}	0.43 ± 0.01

grain boundaries to the total conductivity of the two systems is instead shown in Fig. 5f and g, respectively. In accordance with the Nyquist plots and resistance values discussed above, LAMGPB exhibits a decreased bulk conductivity alongside a pronounced increase in grain boundary conductivity. In particular, bulk conductivity values of 1.5 × 10^{-5} and 1.7 × 10^{-4} S cm^{-1} are achieved by LAMGPB at −20 °C and 20 °C, respectively. 2.2 × 10^{-5} and 3.5 × 10^{-4} S cm^{-1} are reached for LAGP-comm at the same temperatures (Table 3). Looking at grain boundaries instead, the evaluation based on the brick layer model (BLM) accounts for conductivity values of 5.2 × 10^{-8} and 1.4 × 10^{-6} S cm^{-1} at −20 and 20 °C, respectively, for LAMGPB. At the same temperatures, much lower values of 2.0 × 10^{-8} and 3.2 × 10^{-7} S cm^{-1} are instead obtained for LAGP-comm. Overall, the enhanced total conductivity of LAMGPB indicates also that large, localized voids, as those observed in Fig. 3, are less impactful on the total ionic conductivity in comparison to the small and abundant widespread voids observed in LAGP-comm. The same influence of pores on conductivity was observed in a previous study carried out by the authors on a mixed LAGTP NASICON-type system, where the effects of powder sinter-crystallization and bulk devitrification were investigated and compared on a given composition [63]. Based on these evidences, exploring alternative UHS sintering

conditions (e.g., shorter sintering durations at the same current or extended durations at a lower current) would be particularly valuable for gaining further insights into optimizing the material's conductivity. Other studies focused on MgO- or B_2O_3-added LAGP systems further evidenced the impact of sintering and the importance of optimizing densification. For instance, Nikodimos et al. [64] reported a conductivity of 7.4×10^{-4} S cm^{-1} at 25 °C for an MgO-added LAGP bulk system. However, studies on analogous systems obtained through conventional powder sintering have shown lower conductivity values: 3.4×10^{-4} S cm^{-1} according to Kim et al. [65] and 1.07×10^{-4} S cm^{-1} according to Kurihara et al. [66], both at 25 °C, and 1.2×10^{-4} S cm^{-1} according to Leo et al. [67] at 100 °C. These findings highlight the impact of the processing conditions on the resulting performances.

Eventually, according to the Arrhenius plots in Fig. 5e, an E_a value of 0.43 ± 0.01 eV was calculated for LAMGPB compared to 0.47 ± 0.05 eV for LAGP-comm, as reported in Table 3, indicating a reduced activation energy for conduction in the former system.

Overall, among the UHS currents enabling to achieve crystallization (i.e., 21, 22 and 23 An as discussed in *Paragraph 3.2*), 22 A yields the highest total ionic conductivity for both LAGP-comm and LAMGPB. In contrast, the highest density values are observed at 21 A, decreasing progressively with the increasing applied current (Tables S2 and S3). These findings suggest that, under UHS treatment, the highest ionic conductivity in NASICON-type systems may be achieved by sintering at an intermediate temperature that both mitigates the swelling observed via HSM and facilitates the grain reorganization and growth necessary for improved ionic conduction.

Despite the yielded conductivity values, both systems treated at 22 A show a total ionic conductivity significantly reduced compared to conventional sintering, along with a decreased relative density. A comparison between the Arrhenius plots of conductivity *vs.* 1000/T achieved through UHS and conventional sintering is provided in Fig. 6 for LAGP-comm and LAMGPB (Fig. 6a and d, respectively). In particular, LAGP-comm achieves a total conductivity of 7.1×10^{-5} S cm^{-1} at 20 °C through conventional sintering (Table 4), against 3.4×10^{-5} S cm^{-1} after UHS treatment at 22 An as discussed above (Table 3). Similarly, the total conductivity value of 6.6×10^{-5} S cm^{-1} at 20 °C for LAMGPB treated at 22 A (Table 3) is lower compared to the 1.2×10^{-4} S cm^{-1} (Table 4) reached at the same temperature through conventional sintering. Despite the significant decrease, this trend is aligned with the

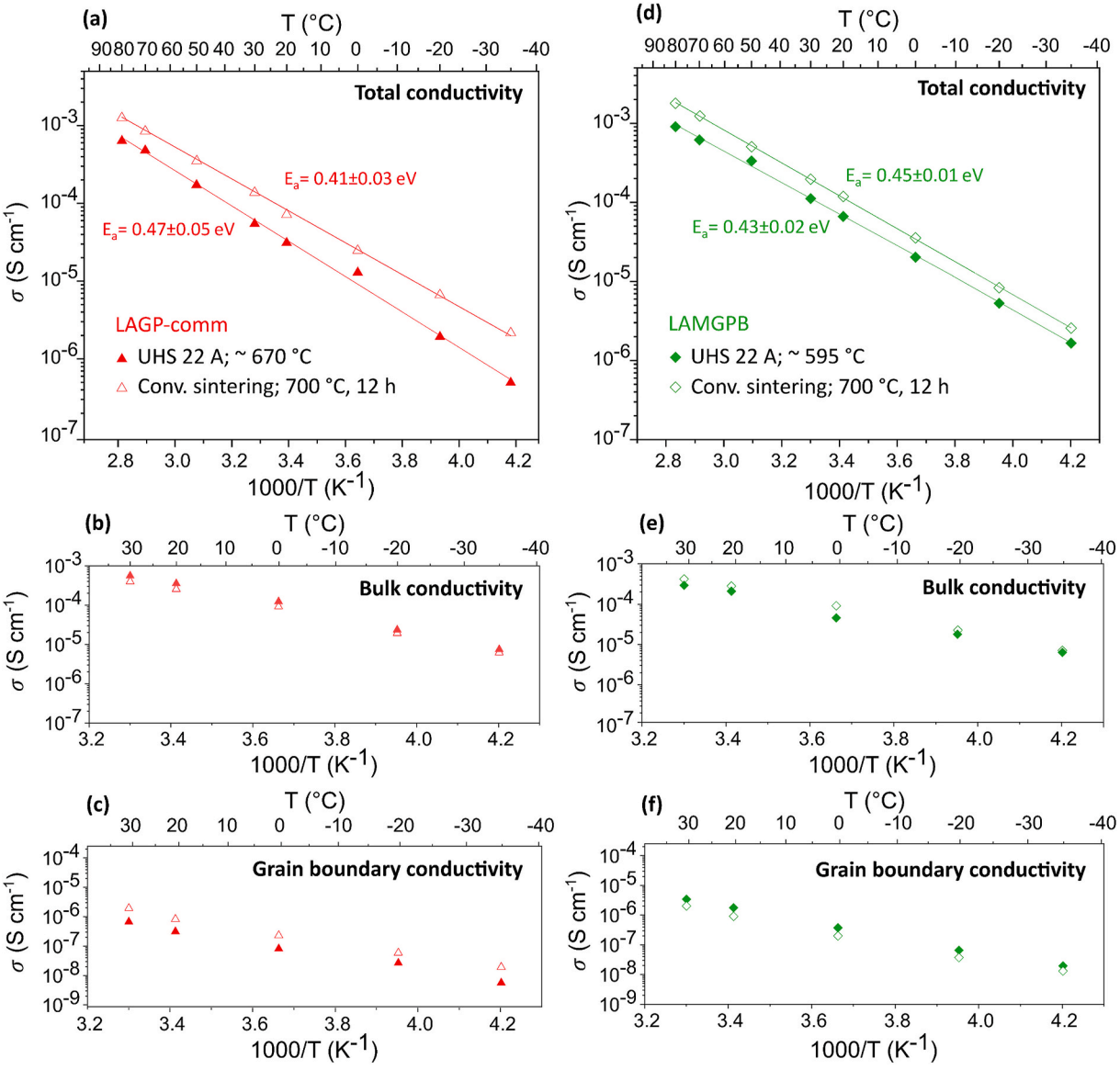

Fig. 6. Arrhenius plots of the total **(a,d)**, bulk **(b,e)** and grain boundary **(c,f)** conductivities of LAGP-comm and LAMGPB, respectively, sintered through UHS at 22 A in comparison with conventional sintering (700 °C, 12 h).

Table 4
Total, bulk and grain boundary conductivity values (S cm^{-1}) measured at −20 °C and 20 °C for LAGP-comm and LAMGPB amorphous powders sintered through conventional sintering. The activation energy for the two systems is also reported.

Sample	Ionic conductivity @ −20 °C (S cm^{-1})			Ionic conductivity @ 20 °C (S cm^{-1})			E_a (eV)
	σ_{tot}	σ_{bulk}	σ_{gb}	σ_{tot}	σ_{bulk}	σ_{gb}	
LAGP comm – Conv. Sintering	8.1 × 10^{-6}	1.9 × 10^{-5}	3.5 × 10^{-8}	7.1 × 10^{-5}	1.7 × 10^{-4}	4.0 × 10^{-7}	0.41 ± 0.03
LAMGPB – Conv. Sintering	8.3 × 10^{-6}	2.2 × 10^{-5}	4.8 × 10^{-8}	1.2 × 10^{-4}	2.8 × 10^{-4}	9.1 × 10^{-7}	0.45 ± 0.01

behavior observed by Curcio et al. [30], who reported a halving in the values of ionic conductivity from conventional sintering to UHS. However, as evidenced by the conductivity values reported in Tables 3 and 4, it is noteworthy to highlight that the total conductivity of LAMGPB is doubled compared to that of LAGP-comm upon treatment by both UHS and conventional sintering, proving the positive effect of adding B_2O_3 within the glass composition. Moreover, the decrease in total conductivity from conventional sintering to UHS is less pronounced for LAMGPB (−45 %) compared to LAGP-comm (−51 %). By looking at grain boundary contributions, LAGP-comm shows decreased σ_{gb} when treated through UHS rather than conventional sintering. At 20 °C, a value of 2.6 × 10^{-7} S cm^{-1} is in fact reached compared to 4.0 × 10^{-7} S cm^{-1}, respectively, indicating a negative effect of UHS on grain boundaries for this system. On the contrary, an improvement from 9.10 × 10^{-7} to 1.4 × 10^{-6} S cm^{-1} is observed for LAMGPB. This result is noteworthy of attention, as it evidences that, under treatment through UHS, grain boundaries are effectively improved by use of a modified LAGP composition such as LAMGPB.

4. Conclusions

In the present study, the B_2O_3-added (LAMGPB) system was produced via melt-casting and the UHS sintering of its amorphous powders was investigated through UHS in comparison with commercial amorphous LAGP. Thermal analyses revealed an increased glass stability for the LAMGPB system, enabling an improved decoupling of densification and crystallization under increasing heating rates, as achieved through UHS. Currents in the range from 19 to 23 A were investigated for sintering, revealing a maximum densification for the amorphous samples at 20 A, prior to crystallization. At 21 A and above, both systems crystallized into the main LAGP ion-conducting phase and pores appeared across the structures. An increase in volume % was indeed registered above 700 °C through HSM, evidencing the swelling behavior typically observed for glassy systems as a result of the trapping of gases that occurs during melt-casting. Notably, no secondary phases associated to lithium loss (i.e. GeO_2 and $AlPO_4$) were observed in both crystalline systems, as opposed to conventional sintering which conversely induced the formation of GeO_2 in LAMGPB. This confirmed the positive impact of fast heating through UHS. From a microstructural point of view, FESEM and TEM-EDX analyses highlighted the segregation of an Al/Ge/P-poor amorphous-like secondary phase at the grain boundary in the LAMGPB samples, attributable to B_2O_3. This amorphous oxide is reported to melt at about 450 °C improving grain growth and cohesion, two features that were indeed observed in LAMGPB in contrast to commercial LAGP. Eventually, EIS analysis showed an improved total ionic-conductivity for LAMGPB, with a value of 6.6 × 10^{-5} S cm^{-1} at 20 °C compared to 3.4 × 10^{-5} for commercial LAGP at the same temperature. This increase (doubled) could be attributed to an improved grain boundary conductivity value of 1.4 × 10^{-6} S cm^{-1} compared to 3.2 × 10^{-7} S cm^{-1}, respectively. Overall, this study evidences the importance of using sintering aids to improve lithium-ion transport at the grain boundary of NASICON-type electrolytes, not only under conventional sintering but also upon the use of UHS. Most importantly, the possibility and effectiveness of directly incorporating these aids into the glass composition is reported, which is particularly relevant in simplifying the preparation in view of its practical application in commercial devices.

CRediT authorship contribution statement

Sofia Saffirio: Writing – review & editing, Writing – original draft, Visualization, Investigation, Formal analysis, Data curation. **Antonio Gianfranco Sabato:** Writing – review & editing, Validation, Supervision, Resources, Project administration, Methodology, Funding acquisition, Conceptualization. **Daiana Marcia Ferreira:** Investigation. **Albert Tarancón:** Writing – review & editing, Validation, Resources, Project administration, Funding acquisition, Conceptualization. **Claudio Gerbaldi:** Writing – review & editing, Validation, Resources, Funding acquisition, Conceptualization. **Federico Smeacetto:** Writing – review & editing, Validation, Resources, Funding acquisition, Conceptualization.

Declaration of competing interest

The authors declare that they have no known competing financial interests or personal relationships that could have appeared to influence the work reported in this paper.

Acknowledgements

This study was carried out under the National Recovery and Resilience Plan (NRRP), within the MOST – Sustainable Mobility Center and received funding from the European Union Next-GenerationEU (PIANO NAZIONALE DI RIPRESA E RESILIENZA – PNRR eMission 4, Component 2, Investment 1.4 and D.D. 1033 June 17, 2022 of the Ministero dell'Università e della Ricerca (MUR), CN00000023). The authors would also like to acknowledge the projects FASSION3D (PID2022-137626OB-C32 funded by MCIU/AEI/10.13039/501100011033/FEDER, UE) and 3DSTORE (PLEC2022-009412, funded by MCIU/AEI/10.13039/501100011033 and by European Union « NextGenerationEU/PRTR). Part of the results are also part of A.G. Sabato's Ramon y Cajal fellowship (RYC2021-034470-I, funded by MCIU/AEI/10.13039/501100011033 and by European Union NextGenerationEU»/PRTR). This manuscript reflects only the authors' views and opinions, neither the European Union nor the European Commission can be considered responsible for them.

Appendix A. Supplementary data

Supplementary data to this article can be found online at https://doi.org/10.1016/j.jpowsour.2025.236768.

Data availability

Data will be made available on request.

References

[1] X. Liang, Q. Pang, I.R. Kochetkov, M.S. Sempere, H. Huang, X. Sun, L.F. Nazar, A facile surface chemistry route to a stabilized lithium metal anode, Nat. Energy 2 (2017) 17119, https://doi.org/10.1038/nenergy.2017.119.
[2] Y.-C. Kim, K.-N. Jung, J.-W. Lee, M.-S. Park, Improving the ionic conductivity of Li1+xAlxGe2-x(PO4)3 solid electrolyte for all-solid-state batteries using microstructural modifiers, Ceram. Int. 46 (2020) 23200–23207, https://doi.org/10.1016/j.ceramint.2020.06.101.
[3] Y. Liu, C. Li, B. Li, H. Song, Z. Cheng, M. Chen, P. He, H. Zhou, Germanium thin film protected lithium aluminum germanium phosphate for solid-state Li batteries, Adv. Energy Mater. 8 (2018) 1702374, https://doi.org/10.1002/aenm.201702374.

[4] J.S. Thokchom, B. Kumar, The effects of crystallization parameters on the ionic conductivity of a lithium aluminum germanium phosphate glass–ceramic, J. Power Sources 195 (2010) 2870–2876, https://doi.org/10.1016/j.jpowsour.2009.11.037.

[5] Z. Sun, L. Liu, Y. Lu, G. Shi, J. Li, L. Ma, J. Zhao, H. An, Preparation and ionic conduction of Li1.5Al0.5Ge1.5(PO4)3 solid electrolyte using inorganic germanium as precursor, J. Eur. Ceram. Soc. 39 (2019) 402–408, https://doi.org/10.1016/j.jeurceramsoc.2018.09.025.

[6] Q. Liu, Q. Yu, S. Li, S. Wang, L. Zhang, B. Cai, D. Zhou, B. Li, Safe LAGP-based all solid-state Li metal batteries with plastic super-conductive interlayer enabled by in-situ solidification, Energy Storage Mater. 25 (2020) 613–620, https://doi.org/10.1016/j.ensm.2019.09.023.

[7] M. Zhang, K. Takahashi, N. Imanishi, Y. Takeda, O. Yamamoto, B. Chi, J. Pu, J. Li, Preparation and electrochemical properties of Li1+xAlxGe2-x(PO4)3 synthesized by a sol-gel method, J. Electrochem. Soc. 159 (2012) A1114, https://doi.org/10.1149/2.080207jes.

[8] Y. Liu, J. Liu, Q. Sun, D. Wang, K.R. Adair, J. Liang, C. Zhang, L. Zhang, S. Lu, H. Huang, et al., Insight into the microstructure and ionic conductivity of cold sintered NASICON solid electrolyte for solid-state batteries, ACS Appl. Mater. Interfaces 11 (2019) 27890–27896, https://doi.org/10.1021/acsami.9b08132.

[9] B. Yan, L. Kang, M. Kotobuki, L. He, B. Liu, K. Jiang, Boron group element doping of Li1.5Al0.5Ge1.5(PO4)3 based on microwave sintering, J. Solid State Electrochem. 25 (2021) 527–534, https://doi.org/10.1007/s10008-020-04829-2.

[10] H. Tong, J. Liu, J. Liu, Y. Liu, D. Wang, X. Sun, X. Song, Microstructure and ionic conductivity of Li1.5Al0.5Ge1.5(PO4)3 solid electrolyte prepared by spark plasma sintering, Ceram. Int. 46 (2020) 7634–7641, https://doi.org/10.1016/j.ceramint.2019.11.264.

[11] Y. Zhu, T. Wu, J. Sun, M. Kotobuki, Highly conductive lithium aluminum germanium phosphate solid electrolyte prepared by sol-gel method and hot-pressing, Solid State Ionics 350 (2020) 115320, https://doi.org/10.1016/j.ssi.2020.115320.

[12] R.R. Mishra, A.K. Sharma, Microwave–material interaction phenomena: heating mechanisms, challenges and opportunities in material processing, Compos. Appl. Sci. Manuf. 81 (2016) 78–97, https://doi.org/10.1016/j.compositesa.2015.10.035.

[13] M. Oghbaei, O. Mirzaee, Microwave versus conventional sintering: a review of fundamentals, advantages and applications, J. Alloys Compd. 494 (2010) 175–189, https://doi.org/10.1016/j.jallcom.2010.01.068.

[14] O. Guillon, J. Gonzalez-Julian, B. Dargatz, T. Kessel, G. Schierning, J. Räthel, M. Herrmann, Field-assisted sintering technology/spark plasma sintering: mechanisms, materials, and technology developments, Adv. Eng. Mater. 16 (2014) 830–849, https://doi.org/10.1002/adem.201300409.

[15] C. Wang, W. Ping, Q. Bai, H. Cui, R. Hensleigh, R. Wang, A.H. Brozena, Z. Xu, J. Dai, Y. Pei, et al., A general method to synthesize and sinter bulk ceramics in seconds, Science 368 (2020) 521–526, https://doi.org/10.1126/science.aaz7681.

[16] M. Kermani, D. Zhu, J. Li, J. Wu, Y. Lin, Z. Dai, C. Hu, S. Grasso, Ultra-fast high-temperature sintering (UHS) of translucent alumina, Open Ceramics 9 (2022) 100202, https://doi.org/10.1016/j.oceram.2021.100202.

[17] J. Dong, V. Pouchly, M. Biesuz, V. Tyrpekl, M. Vilémová, M. Kermani, M. Reece, C. Hu, S. Grasso, Thermally-insulated ultra-fast high temperature sintering (UHS) of zirconia: a master sintering curve analysis, Scr. Mater. 203 (2021) 114076, https://doi.org/10.1016/j.scriptamat.2021.114076.

[18] M.J.-H. Reavley, H. Guo, J. Yuan, A.Y.R. Ng, T.Y.K. Ho, H.T. Tan, Z. Du, C.L. Gan, Ultrafast high-temperature sintering of barium titanate ceramics with colossal dielectric constants, J. Eur. Ceram. Soc. 42 (2022) 4934–4943, https://doi.org/10.1016/j.jeurceramsoc.2022.04.056.

[19] T.P. Mishra, S. Wang, C. Lenser, D. Jennings, M. Kindelmann, W. Rheinheimer, C. Broeckmann, M. Bram, O. Guillon, Ultra-fast high-temperature sintering of strontium titanate, Acta Mater. 231 (2022) 117918, https://doi.org/10.1016/j.actamat.2022.117918.

[20] M. Ihrig, T.P. Mishra, W.S. Scheld, G. Häuschen, W. Rheinheimer, M. Bram, M. Finsterbusch, O. Guillon, Li7La3Zr2O12 solid electrolyte sintered by the ultrafast high-temperature method, J. Eur. Ceram. Soc. 41 (2021) 6075–6079, https://doi.org/10.1016/j.jeurceramsoc.2021.05.041.

[21] M. Biesuz, A. Galotta, A. Motta, M. Kermani, S. Grasso, J. Vontorová, V. Tyrpekl, M. Vilémová, V.M. Sglavo, Speedy bioceramics: rapid densification of tricalcium phosphate by ultrafast high-temperature sintering, Mater. Sci. Eng. C 127 (2021) 112246, https://doi.org/10.1016/j.msec.2021.112246.

[22] L. Spiridigliozzi, G. Dell'Agli, S. Esposito, P. Rivolo, S. Grasso, V.M. Sglavo, M. Biesuz, Ultra-fast high-temperature sintering (UHS) of Ce0.2Zr0.2Y0.2Gd0.2La0.2O2−δ fluorite-structured entropy-stabilized oxide (F-eso), Scr. Mater. 214 (2022) 114655, https://doi.org/10.1016/j.scriptamat.2022.114655.

[23] S. Boldrini, A. Ferrario, S. Fasolin, A. Miozzo, S. Barison, Ultrafast high-temperature sintering and thermoelectric properties of n-doped Mg2Si, Nanotechnology 34 (2023) 155601, https://doi.org/10.1088/1361-6528/acb15a.

[24] H.W. Li, Y.P. Zhao, G.Q. Chen, M.H. Li, Z.F. Wei, X.S. Fu, W.L. Zhou, SiC-based ceramics with remarkable electrical conductivity prepared by ultrafast high-temperature sintering, J. Eur. Ceram. Soc. 43 (2023) 2269–2274, https://doi.org/10.1016/j.jeurceramsoc.2022.12.025.

[25] J. Wu, Y. Lin, C. Hu, S. Grasso, D. Zhu, J. Li, A. Katz-Demyanitcz, A. Goldstein, Ultra-fast high-temperature sintering of transparent MgAl2O4, Ceram. Int. 49 (2023) 19537–19540, https://doi.org/10.1016/j.ceramint.2023.03.018.

[26] S. Wang, T.P. Mishra, Y. Deng, L. Balice, A. Kaletsch, M. Bram, C. Broeckmann, Electric current-assisted sintering of 8YSZ: a comparative study of ultrafast high-temperature sintering and flash sintering, Adv. Eng. Mater. 25 (2023) 2300145, https://doi.org/10.1002/adem.202300145.

[27] Z. Sun, W. Fan, Y. Bai, A flexible method to fabricate exsolution-based nanoparticle-decorated materials in seconds, Adv. Sci. 9 (2022) 2200250, https://doi.org/10.1002/advs.202200250.

[28] A. Curcio, M.J. Robson, A. Belotti, Z. Hu, Y.-Y. Chin, C.-T. Chen, H.-J. Lin, F. Ciucci, Enhanced electrocatalysts fabricated via quenched ultrafast sintering: physicochemical properties and water oxidation applications, Adv. Mater. Interfac. 9 (2022) 2102228, https://doi.org/10.1002/admi.202102228.

[29] Y. Lin, N. Luo, E. Quattrocchi, F. Ciucci, J. Wu, M. Kermani, J. Dong, C. Hu, S. Grasso, Ultrafast high-temperature sintering (UHS) of Li1.3Al0.3Ti1.7(PO4)3, Ceram. Int. 47 (2021) 21982–21987, https://doi.org/10.1016/j.ceramint.2021.04.216.

[30] A. Curcio, A.G. Sabato, M. Nuñez Eroles, J.C. Gonzalez-Rosillo, A. Morata, A. Tarancón, F. Ciucci, Ultrafast crystallization and sintering of Li1.5Al0.5Ge1.5(PO4)3 glass and its impact on ion conduction, ACS Appl. Energy Mater. 5 (2022) 14466–14475, https://doi.org/10.1021/acsaem.2c03009.

[31] J. Wu, Y. Lin, M. Kermani, C. Hu, S. Grasso, Ultra-fast high temperature sintering (UHS) of Li1.5Al0.5Ge1.5P3O12 electrolyte: a rationalization of the heating schedule, Ceram. Int. 48 (2022) 6356–6362, https://doi.org/10.1016/j.ceramint.2021.11.178.

[32] J. Wu, M. Kermani, L. Cao, B. Wang, Z. Dai, L. Fu, C. Hu, S. Grasso, Rapid crystallization of Li1.5Al0.5Ge1.5(PO4)3 glass ceramics via ultra-fast high-temperature sintering (UHS), Int. J. Appl. Ceram. Technol. 20 (2023) 2125–2130, https://doi.org/10.1111/ijac.14355.

[33] S.V. Pershina, T.A. Kuznetsova, E.G. Vovkotrub, S.A. Belyakov, E.S. Kuznetsova, Solid electrolyte membranes based on Li2O–Al2O3–GeO2–SiO2–P2O5 glasses for all-solid state batteries, Membranes 12 (2022) 1245, https://doi.org/10.3390/membranes12121245.

[34] D.H. Kothari, D.K. Kanchan, Effect of doping of trivalent cations Ga3+, Sc3+, Y3+ in Li1.3Al0.3Ti1.7 (PO4)3 (LATP) system on Li+ ion conductivity, Phys. B Condens. Matter 501 (2016) 90–94, https://doi.org/10.1016/j.physb.2016.08.020.

[35] P. Goharian, B. Eftekhari Yekta, A.R. Aghaei, S. Banijamali, Lithium ion-conducting glass-ceramics in the system Li2O–TiO2–P2O5–Cr2O3–SiO2, J. Non-Cryst. Solids 409 (2015) 120–125, https://doi.org/10.1016/j.jnoncrysol.2014.11.016.

[36] Y. Nikodimos, L.H. Abrha, H.H. Weldeyohannes, K.N. Shitaw, N.T. Temesgen, B. W. Olbasa, C.-J. Huang, S.-K. Jiang, C.-H. Wang, H.-S. Sheu, et al., A new high-Li+-Conductivity Mg-doped Li1.5Al0.5Ge1.5(PO4)3 solid electrolyte with enhanced electrochemical performance for solid-state lithium metal batteries, J. Mater. Chem. A 8 (2020) 26055–26065, https://doi.org/10.1039/D0TA07807G.

[37] A. Das, M. Goswami, M. Krishnan, Study on electrical and structural properties in SiO2 substituted Li2O-Al2O3-GeO2-P2O5 glass-ceramic systems, Ceram. Int. 44 (2018) 13373–13380, https://doi.org/10.1016/j.ceramint.2018.04.172.

[38] V.A. Vizgalov, T. Nestler, L.A. Trusov, I.A. Bobrikov, O.I. Ivankov, M.V. Avdeev, M. Motylenko, E. Brendler, A. Vyalikh, D.C. Meyer, et al., Enhancing lithium-ion conductivity in NASICON glass-ceramics by adding yttria, CrystEngComm 20 (2018) 1375–1382, https://doi.org/10.1039/C7CE01910F.

[39] S. Saffirio, H. Darjazi, M.E. Coller Pascuzzi, F. Smeacetto, C. Gerbaldi, Melt-casted Li1.5Al0.3Mg0.1Ge1.6(PO4)3 glass ceramic electrolytes: a comparative study on the effect of different oxide doping, Heliyon 10 (2024) e24493, https://doi.org/10.1016/j.heliyon.2024.e24493.

[40] A.K. Varshneya, J.C. Mauro, Glass compositions and structures, in: Fundamentals of Inorganic Glasses, Elsevier, 2019, pp. 101–164.

[41] M.N. Rahaman, Sintering of Ceramics, CRC, Boca Raton, 2008.

[42] A. Norouzi, S. Banijamali, A. Keshavarzi, Sinter-crystallization, phase development and microstructural evaluations of ZnO containing 45S5® glass-ceramics, Mater. Today Proc. 5 (2018) 15696–15701, https://doi.org/10.1016/j.matpr.2018.04.180.

[43] J.A. Dias, S.H. Santagneli, Y. Messaddeq, Methods for lithium ion NASICON preparation: from solid-state synthesis to highly conductive glass-ceramics, J. Phys. Chem. C 124 (2020) 26518–26539, https://doi.org/10.1021/acs.jpcc.0c07385.

[44] J. Jiusti, E.D. Zanotto, S.A. Feller, H.J. Austin, H.M. Detar, I. Bishop, D. Manzani, Y. Nakatsuka, Y. Watanabe, H. Inoue, Effect of network formers and modifiers on the crystallization resistance of oxide glasses, J. Non-Cryst. Solids 550 (2020) 120359, https://doi.org/10.1016/j.jnoncrysol.2020.120359.

[45] S.V. Pershina, E.G. Vovkotrub, B.D. Antonov, Effects of B_2O_3 on crystallization kinetics, microstructure and properties of $Li_{1.5}Al_{0.5}Ge_{1.5}(PO_4)_3$-based glass-ceramics, Solid State Ionics 383 (2022) 115990, https://doi.org/10.1016/j.ssi.2022.115990.

[46] M. Leśniak, R. Szal, B. Starzyk, M. Gajek, M. Kochanowicz, J. Żmojda, P. Miluski, J. Dorosz, M. Sitarz, D. Dorosz, Influence of barium oxide on glass-forming ability and glass stability of the tellurite–phosphate oxide glasses, J. Therm. Anal. Calorim. 138 (2019) 4295–4302, https://doi.org/10.1007/s10973-019-08715-6.

[47] F. Smeacetto, M. Radaelli, M. Salvo, D. Di Modugno, A.G. Sabato, V. Casalegno, M. Broglia, M. Ferraris, Glass-ceramic joining material for sodium-based battery, Ceram. Int. 43 (2017) 8329–8333, https://doi.org/10.1016/j.ceramint.2017.03.170.

[48] P.-H. Kuo, J. Du, Crystallization behavior of Li1+xAlxGe2-x(PO4)3 glass-ceramics: effect of composition and thermal treatment, J. Non-Cryst. Solids 525 (2019) 119680, https://doi.org/10.1016/j.jnoncrysol.2019.119680.

[49] M. Bertrand, S. Rousselot, M. Rioux, D. Aymé-Perrot, M. Dollé, Concurrent crystallization mechanism leading to low temperature percolation of LAGP glass-ceramic electrolyte, ACS Appl. Mater. Interfaces 16 (2024) 28818–28828, https://doi.org/10.1021/acsami.4c03003.

[50] M. Chu, M.N. Rahaman, L.C. De Jonghe, R.J. Brook, Effect of heating rate on sintering and coarsening, J. Am. Ceram. Soc. 74 (1991) 1217–1225, https://doi.org/10.1111/j.1151-2916.1991.tb04090.x.

[51] R. Monroe, Porosity in castings, ChemInform 37 (2006), https://doi.org/10.1002/chin.200642218.
[52] E. Yang, T. Ding, T. Ren, Effect of casting temperature control on microstructure and properties of continuously cast Zr-based bulk metallic glass slabs, Coatings 14 (2024) 747, https://doi.org/10.3390/coatings14060747.
[53] M. Biesuz, L. Karacasulu, C. Vakifahmetoglu, V.M. Sglavo, On the temperature measurement during ultrafast high-temperature sintering (UHS): shall we trust metal-shielded thermocouples? J. Eur. Ceram. Soc. 44 (2024) 3479–3485, https://doi.org/10.1016/j.jeurceramsoc.2023.11.061.
[54] F. Zuo, Q. Wang, Z.-Q. Yan, M. Kermani, S. Grasso, G.-L. Nie, B.-B. Jiang, F.-P. He, H.-T. Lin, L.-G. Wang, Upscaling ultrafast high-temperature sintering (UHS) to consolidate large-sized and complex-shaped ceramics, Scr. Mater. 221 (2022) 114973, https://doi.org/10.1016/j.scriptamat.2022.114973.
[55] A.M. Cruz, E.B. Ferreira, A.C.M. Rodrigues, Controlled crystallization and ionic conductivity of a nanostructured LiAlGePO4 glass–ceramic, J. Non-Cryst. Solids 355 (2009) 2295–2301, https://doi.org/10.1016/j.jnoncrysol.2009.07.012.
[56] E.I. Burmakin, G.S. Shehtman, V.N. Alikin, Ionic conductivity of Li6Ge2O7 and its solid solutions, Mater. Sci. Forum 76 (1991) 107–110. http://doi.org/10.4028/www.scientific.net/MSF.76.107.
[57] F.A.L. Laskowski, D.B. McHaffie, K.A. See, Identification of potential solid-state Li-ion conductors with semi-supervised learning, Energy Environ. Sci. 16 (2023) 1264–1276, https://doi.org/10.1039/D2EE03499A.
[58] S. Yao, L. Xuemi, Z. Wanjun, Y. Xiaodan, W. Yuanyi, Z. Zhuomin, L. Shiyuan, X. Xiaote, Y. Zhengbao, Programmable and rapid fabrication of complex-shape ceramics, Nat. Commun. 15 (2024) 9973, https://doi.org/10.1038/s41467-024-54393-w.
[59] S. Bhandari, O. Hanzel, M. Kermani, V.M. Sglavo, M. Biesuz, G. Franchin, Rapid debinding and sintering of alumina ceramics fabricated by direct ink writing, J. Eur. Ceram. Soc. 45 (2025) 117144, https://doi.org/10.1016/j.jeurceramsoc.2024.117144.
[60] S. Bhandari, O. Hanzel, P. Veteska, M. Janek, E. De Bona, V.M. Sglavo, M. Biesuz, G. Franchin, From rapid prototyping to rapid firing: on the feasibility of high-speed production for complex $BaTiO_3$ components, J. Am. Ceram. Soc. 107 (2024) 6562–6573, https://doi.org/10.1111/jace.19950.
[61] C.R. Mariappan, C. Yada, F. Rosciano, B. Roling, Correlation between micro-structural properties and ionic conductivity of Li1.5Al0.5Ge1.5(PO4)3 ceramics, J. Power Sources 196 (2011) 6456–6464, https://doi.org/10.1016/j.jpowsour.2011.03.065.
[62] S. Breuer, D. Prutsch, Q. Ma, V. Epp, F. Preishuber-Pflügl, F. Tietz, M. Wilkening, Separating bulk from grain boundary Li ion conductivity in the sol–gel prepared solid electrolyte Li1.5Al0.5Ti1.5(PO4)3, J. Mater. Chem. A 3 (2015) 21343–21350, https://doi.org/10.1039/C5TA06379E.
[63] S. Saffirio, M. Falco, G.B. Appetecchi, F. Smeacetto, C. Gerbaldi, Li1.4Al0.4Ge0.4Ti1.4(PO4)3 promising NASICON-structured glass-ceramic electrolyte for all-solid-state Li-based batteries: unravelling the effect of diboron trioxide, J. Eur. Ceram. Soc. 42 (2022) 1023–1032, https://doi.org/10.1016/j.jeurceramsoc.2021.11.014.
[64] Y. Nikodimos, L.H. Abrha, H.H. Weldeyohannes, K.N. Shitaw, N.T. Temesgen, B. W. Olbasa, C. Huang, S. Jiang, C. Wang, H. Sheu, S. Wu, W. Su, C. Yang, B. J. Hwang, A new high-Li+-conductivity Mg-doped Li1.5Al0.5Ge1.5(PO4)3 solid electrolyte with enhanced electrochemical performance for solid-state, J. Mater. Chem. A 8 (2020) 26055–26065, https://doi.org/10.1039/d0ta07807g.
[65] Y. Kim, K. Jung, J. Lee, M. Park, Improving the ionic conductivity of $Li_{1+x}Al_xGe_{2-x}(PO_4)_3$ solid electrolyte for all-solid-state batteries using microstructural modifiers, Ceram. Int. 46 (2020) 23200–23207, https://doi.org/10.1016/j.ceramint.2020.06.101.
[66] R. Kurihara, N. Shinada, H. Morimoto, Lithium ion conductivities of solid electrolytes prepared by low- temperature heat treatment of amorphous materials in the Li_2O-Al_2O_3-GeO_2-P_2O_5 system for all-solid-state batteries, Electrochemistry 91 (2023) 037010, https://doi.org/10.5796/electrochemistry.23-00020.
[67] C.J. Leo, G.V. Subba Rao, B.V.R. Chowdari, Effect of MgO addition on the ionic conductivity of LiGe2(PO4)3 ceramics, Solid State Ionics 159 (2003) 357–367, https://doi.org/10.1016/S0167-2738(03)00032-8.